Journal of Materials Chemistry A

REVIEW

View Article Online
View Journal | View Issue

Cite this: J. Mater. Chem. A, 2025, 13, 27794

3D-printed lattice structures for thermoelectric devices – a review

Spyridon N. Katsantonis *[ab] and Christos Tsamis *[b]

Energy harvesting technologies are becoming increasingly important due to the growing energy demand. Waste heat is a form of energy that remains largely unexploited and could be utilised by thermoelectric devices. Thermoelectric generators have the ability to convert heat into electricity. Traditionally, thermoelectric generators consist of thermoelectric legs with bulk structures, whose fabrication includes multiple steps. Additive manufacturing techniques, which are popularly known as 3D-printing, have the potential to simplify these time-consuming and cost-intensive fabrication processes, while providing flexibility in design and reducing waste material. The freedom of design that 3D-printing techniques provide, allows new architectures, like lattice structures, to be investigated as legs in thermoelectric devices. Lattice structures could assist in the decoupling of competing thermoelectric properties of the materials. The aim of this paper is to review the application of 3D-printed lattice structures in thermoelectric devices and to highlight the advantages of lattice architectures for improving the perfomance of thermoelectric devices.

Received 2nd March 2025
Accepted 25th July 2025

DOI: 10.1039/d5ta01722j

rsc.li/materials-a

1. Introduction

Increasing energy demand due to rapid societal and energy-intensive developments drives innovation in the field of energy harvesting. Particular attention has been given to finding ways to produce and recycle energy more efficiently. Thus, many technologies have been developed to harvest energy from sustainable sources (*e.g.* solar energy, wind power, hydroelectric power). Another form of energy that remains largely unexploited is waste heat. Heat gradients generated by natural phenomena or industrial processes could be utilized to produce energy through the application of the thermoelectric effect, also known as Seebeck effect. Thermoelectric materials have the unique ability to convert heat into electric energy. Traditionally, Bi_2Te_3-based materials have been extensively used in thermoelectric devices particularly at low temperatures (300–400 K) due to their

[a]Department of Chemical Sciences, School of Chemical Engineering, National Technical University of Athens, 9 Iroon Polytechniou Str., Athens, 15772, Greece. E-mail: s.katsantonis@inn.demokritos.gr
[b]Institute of Nanoscience and Nanotechnology, National Center for Scientific Research 'Demokritos', Athens, 15310, Greece. E-mail: c.tsamis@inn.demokritos.gr

Spyridon N. Katsantonis

Spyridon N. Katsantonis received his Diploma (MEng) in Chemical Engineering from the National Technical University of Athens (NTUA). He is currently a PhD candidate at NTUA and conducts his research in collaboration with NCSR "Demokritos". His main research interests revolve around the synthesis of thermoelectric nanomaterials for 3D printing applications as well as the design and fabrication of thermoelectric generators.

Dr Christos Tsamis

Dr Christos Tsamis is Director of Research at the Inst. of Nanoscience & Nanotechnology at the National Center for Scientific Research "Demokritos", leading the group on "Energy Harvesting and Autonomous Sensors". His research interests focus on Micro- and Nanofabrication technologies for Microsystems for devices and sensors, Nanostructured materials and devices for Energy harvesting, Chemical Sensors and flexible electronics. He is the author or co-author of over 200 publications in peer-reviewed International Journals, Conference Proceedings, and contributions in International Conferences.

good thermoelectric properties and high efficiency.[1,2] However, these inorganic materials, *e.g.* Bi_2Te_3, exhibit many drawbacks in terms of toxicity, scarcity, brittleness and high cost.

On the other hand, modern advanced applications require materials with multiple functionalities, which sometimes are antagonistic, such as light weight in combination with high strength or high electrical conductivity with low thermal conductivity and *vice versa*. This issue has been addressed mostly at the chemical level by the synthesis of hybrid materials (*e.g.* doping) or composite materials (*e.g.* polymer-matrix composites). Nevertheless, the multi-functionality of the materials could alternatively be approached through the architecture of structural units. Lattice architectures not only reduce the weight of the structures, but also the cost and sourcing of raw materials. The advantages and improved thermoelectric performance that arise by altering the bulk, not only microstructure of thin thermoelectric films,[3] but also architecture and geometry of the components in thermoelectric devices, have been studied both experimentally[4] and numerically.[5] However, many design constraints derive from the existing manufacturing processes, which limit the topologies and the feature size of the fabricated structures.

In this context, printing methods can be very useful for manufacturing structures with complex geometries. Depending on the printing method that is being utilised, the result could be either a 2D or a 3D structure. Printing techniques, such as inkjet printing, screen printing, aerosol jet printing *etc.* typically result in 2D structures, in the form of thin films. However, there have been some recent attempts, where 3D structures (*e.g.* lattice structures) have been successfully fabricated by inkjet printing[6] and aerosol jet printing.[7,8] On the contrary, additive manufacturing techniques, such as stereolithography, selective-laser sintering and two-photon vat photopolymerization, enable the fabrication of 3D structures with feature sizes down to 100 μm or even smaller,[9,10] while providing topological freedom. Apart from flexibility in design and customization, additive manufacturing techniques can reduce the number of processes and quantity of materials that are required for the fabrication of 3D-structures. Further information about the different printing techniques, printable thermoelectric materials and devices can be found in recent review papers.[11–15]

The aim of this paper is to highlight the importance of lattice structures fabricated through additive manufacturing techniques and their application in thermoelectric devices *via* 3D-printing. While there are several review articles that study the production of 3D-printed thermoelectric devices, most address only bulk thermoelectric components. In contrast, this review specifically focuses on the fabrication and characterization of 3D-printed lattice thermoelectric devices.

We begin with a concise overview of the 3D-printing methods employed in the creation of lattice structures, followed by a survey of the thermoelectric materials used in these devices. Subsequently, we discuss the 3D lattice structures that serve as the foundation for thermoelectric applications. A thorough analysis of 3D lattice structures is provided, highlighting both their advantages and disadvantages. Finally, we address the challenges and future prospects associated with these technologies.

2. Additive manufacturing

Additive manufacturing (AM) is the formalized term for what is widely known as 3D-printing. Initially, a model is designed with the assistance of a Computer Aided Design (CAD) software and then is transferred to the building machine (printer). The machine needs to be set up properly, since the building process is automated. The part is formed by adding material in layers, according to the parameters that have been ascribed to the model during the design process. Based on the forming process of the 3D structure and the way layers are formed and bonded to each other, AM technologies can be divided into many different categories. Several reviews describe in detail the variety of the existing AM technologies and their characteristics.[16–20] Moreover, emerging trends in the sphere of AM technologies, include electric-, magnetic- and ultrasound-field-assisted 3D-printing techniques, where the layers are formed under the influence of an external stimulus (electric-, magnetic- or acoustic-field). Further information about the various field-assisted 3D-printing techniques and their applications can be found in the literature.[21–24] The AM technologies that have been used hitherto for the fabrication of lattice structures in thermoelectric devices, include material extrusion, vat photopolymerization and powder bed fusion. An overview of the main 3D-printing techniques is provided in Table 1.

2.1 Material extrusion

Material extrusion consists of a continuous layer-by-layer deposition of a fused filament or a viscous ink onto a substrate and can be categorized in fused deposition modelling (FDM) or fused filament fabrication (FFF) and direct ink writing (DIW). A brief description of these techniques follows, while more information can be found in the literature.[25–28] In FDM and FFF, the printing process takes place by melting thermoplastic fused filaments and continuously depositing the molten material onto a substrate, which then solidifies at room temperature in a layer-by-layer manner. Although FDM and FFF are low-cost and high-speed techniques, layer-by-layer appearance and poor surface quality[29] could limit their application. In DIW, the printing ink is placed in a syringe and extruded from a nozzle head using compressed air, in order to form a continuous self-standing filament. The desired 3D structure is formed by manipulating the syringe motion. One of the main advantages of DIW is the diversity of printable materials, including viscous polymer gels and colloidal suspensions.[30,31]

2.2 Vat photopolymerization

In vat photopolymerization, a liquid resin, which is stored in a vat, is selectively cured by a light source (usually UV light), in order to construct layer-by-layer the desired structure. The exposure of the resin to light initiates a chain reaction (polymerization), which leads to solidification. Only the desired pattern of the model is exposed to light and solidifies, thus creating a layer, on top of which subsequent layers will be cured. Vat photopolymerization is often referred to as stereolithography (SLA) or digital light processing (DLP). Many

Table 1 Overview of the main 3D-printing techniques

Technique	Feed material	Method
Fused deposition modelling (FDM)	Polymers (*i.e.* PLA, ABS) in filament form	Layer-by-layer deposition of a fused filament or a viscous ink onto a substrate
Direct ink writing (DIW)	Viscous inks (*i.e.* polymer gels, colloidal suspensions)	Ink is placed in a syringe and extruded from a nozzle head using compressed air
Stereolithography (SLA) Digital light processing (DLP)	Photocurable resins	Liquid resin is stored in a vat and is selectively cured by a light source
Selective-laser melting (SLM)	Metals in powder form	Layer is formed by a laser or electron beam that melts the powder. Excess material is removed by vacuum
Selective-laser sintering (SLS)	Metals and polymers in powder form	

reviews about the operation and process parameters of SLA and DLP exist in the literature.[32–34] The main difference between these two techniques is that SLA uses a laser that traces a layer, while a DLP machine uses a projected light source to cure the entire layer at once. SLA printers trace out a path with a laser and cure the resin along that path. Although it is a slow printing process, SLA can produce high quality structures at a resolution as low as 10 μm.[35] Another technique of vat photopolymerization with high level of precision is two-photon vat photopolymerization (TPP). TPP utilizes a light source with longer wavelength (usually near-infrared) than SLA and DLP. Under threshold conditions, feature size of less than 50 nm can be achieved.[10,36,37]

2.3 Powder bed fusion

In powder bed fusion, an electron beam or a laser beam interacts with a solid material (metal or polymer) in powder form. The powder melts topically and then solidifies quickly in a layer-by-layer manner, where new material rolls on top of previous layers and is being fused. Excess material is then removed by a vacuum. Powder bed fusion can be divided into selective-laser melting (SLM), which is suitable for metal powders, and selective-laser sintering (SLS), which is suitable for polymer, metal and alloy powders. The principles of powder bed fusion techniques are presented in other existing reviews.[38–40] The main difference between the two techniques is that SLM involves complete melting of the material, while the laser in SLS does not fully melt the powder, but the elevated temperature on the surface of the grains results in fusion of the powder particles. Thus, SLM produces structures with better mechanical properties than SLS, which sometimes suffer from instability issues during the phase change of the material (solid–liquid–solid).[41] Moreover, a binder material is usually added in SLS, while SLM can be used without the addition of a binder. Although power bed fusion is a slow process associated with high costs, it can produce complex structures with high quality.

3. Thermoelectric materials

The main properties that distinguish thermoelectric (TE) materials from all other materials are the Seebeck coefficient, electrical and thermal conductivity. The efficiency of a TE material is evaluated by the dimensionless figure of merit (zT), which can be estimated by the following equation:

$$zT = \frac{S^2 \times \sigma \times T}{\kappa}$$

where S is the Seebeck coefficient, σ the electrical conductivity of the material, T the temperature and κ the thermal conductivity of the material. The product of $S^2 \times \sigma$ is called thermoelectric power factor (PF) and expresses the power output of a TE material. Ideally, TE materials should possess a combination of high Seebeck coefficient and electrical conductivity, but low thermal conductivity. All these parameters are a function of the charge carrier concentration but with competing trends. An increase in the charge carrier concentration leads to an increase in the electric and thermal conductivity, but a decrease in the Seebeck coefficient.[42] Moreover, the value of zT is a function of the temperature conditions during the application. Thus, a high average value of zT (zT_{ave}) over a temperature range would be more indicative of the material performance than the peak value of zT at one specific temperature, since during commercial applications there are temperature fluctuations.

For power generation applications, TE materials are utilized in electronic devices that are called thermoelectric generators (TEGs). TEGs comprise of n- and p-type materials, by forming n- and p-type TE legs, which are connected electrically in series and thermally in parallel. Apart from good electrical and thermal contacting, the TE legs should have matched thermal expansion. Thus, important parameters that influence the efficiency, but also mechanical strength and cost of TEGs are the chosen couple of TE materials and the geometrical design of the TE legs. More information about the variety of existing TEGs and their characteristics can be found in recent reviews.[43–46]

Since its discovery by Goldsmid and Douglas,[47] Bi_2Te_3 and later other inorganic materials, such as PbTe and SiGe, dominated the field of TE devices.[48] Apart from inorganic materials, numerous other organic and composite materials have been investigated. The main difference between these classes of materials, regarding their application in TE devices, is their operating temperature range and efficiency. According to their TE characteristics, inorganic materials can operate from low to high temperatures, while organic and composite materials face limitations in terms of stability. Therefore, they are mostly used from low to mid-range temperatures. On the other hand, toxicity issues, scarcity, costly manufacturing procedures and brittleness of inorganic materials shifted the focus on composite or even organic materials, which are more flexible, readily available at a lower cost and less toxic. In the following

Table 2 Examples of n- and p-type TE materials and their TE properties[a]

	Material	Type	S [μV K^{-1}]	zT	PF [μW cm^{-1} K^{-2}]	T [K]	Ref.
n-type	$Bi_2Te_{2.7}Se_{0.3}$	Inorganic	∼−240	1.6	46.1	300	50
	Ag_2Se	Inorganic	−140	0.6	9.87	300	51
	$Sn_{0.94}Bi_{0.06}Se$	Inorganic	∼−375.1	2.2	∼7.5	773	53
	$Mg_{3.3}Y_{0.02}Sb_{1.5}Bi_{0.5}$	Inorganic	∼−240	1.16	∼14	759	54
	$Ca_{2.9}La_{0.1}Co_4O_9$	Inorganic	−172	0.205	2.04	873	55
	$V_{0.87}CoSb$	Inorganic	∼−145	0.58	22	950	56
	Bi_2Se_2S + 0.75 wt% $SbCl_3$	Inorganic	∼−200	1.13	6.59	773	57
	Poly[K_x(Ni-ett)]	Organic	−90	0.3	1.7	298	59
	PDI-3	Organic	−170	—	0.014	—	60
	C_{60} derivative	Organic	∼−250	0.34	∼0.8	393	61
	PVDF/Ni	Composite	∼−27	0.15	2.2	380	62
	PEI/PEDOT/CNTs	Composite	−23	—	0.297	300	63
p-type	$Bi_{0.4}Sb_{1.6}Te_3$	Inorganic	∼222.5	1.8	∼37.6	316	72
	Sb_2Te_3	Inorganic	160	0.3	18	300	73
	$MgAg_{0.97}Sb$	Inorganic	220	0.78	22.8	300	74
	$Ge_{0.95}Bi_{0.05}Te_{1.025}$	Inorganic	∼255	2.4	∼51	773	75
	$Ge_{0.9}Sb_{0.1}Te$	Inorganic	∼250	1.85	∼51	725	76
	Cu_2Se	Inorganic	∼230	1.9	∼17.6	1000	77
	SnSe	Inorganic	307.4	1.7	∼5.1	823	78
	PEDOT	Organic	122	—	0.12	310	79
	PTh	Organic	42.5	0.01	0.088	300	80
	PEDOT:PSS/Bi_2Te_3	Composite	169	0.58	13.5	300	81
	PVDF/Cu_2Se	Composite	14.3	0.04	1.0538	303	82
	PEDOT:PSS/SnSe	Composite	110	0.32	3.8	300	83

[a] Poly[K_x(Ni-ett)]: poly(nickel-ethylenetetrathiolate), PDI: perylene diimide, PVDF: poly(vinylidene fluoride), PEI: polyethyleneimine, PEDOT: poly(3,4-ethylenedioxythiophene), CNTs: carbon nanotubes, PTh: polythiophene, PSS: poly(4-styrenesulfonate).

sections, a variety of n- and p-type TE materials will be briefly discussed. Their TE properties are summarized in Table 2.

3.1 n-type thermoelectric materials

Although n-type Bi_2Te_3 exhibited good TE results, research continued and focused on the development of its alloys. Doping with Se led to higher thermoelectric performance, especially for the n-type $Bi_2Te_{2.7}Se_{0.3}$.[49] Tan *et al.*[50] achieved a zT value of 1.6 at room temperature by depositing an n-type film of $Bi_2Te_{2.7}Se_{0.3}$ on glass substrate by controlling the deposition anisotropy with an external electric field. Moreover, Ding *et al.*[51] prepared an n-type flexible Ag_2Se film on a polyamide substrate, which exhibited a PF of 9.87 μW cm^{-1} K^{-2} at room temperature. For mid to high temperatures, since it has been shown[52] that SnSe exhibits very good p-type TE properties due to its low thermal conductivity, Duong *et al.*[53] synthesized successfully n-type SnSe by Bi-doping. The resulting n-type $Sn_{0.94}Bi_{0.06}Se$ TE material exhibited a zT value of 2.2 at 733 K. In addition, Kihou *et al.*[54] synthesized an n-type Mg_3Sb_2-based TE material by Y-doping, which exhibited a zT value of 1.16 at 759 K. Moreover, Ren and Gou[55] synthesized an n-type La-doped $Ca_3Co_4O_9$, which achieved a zT value of 0.205 at 873 K. Ferluccio *et al.*[56] studied the TE properties of three different half-Heusler materials with the chemical formula of A_xCoSb (A = V, Nb or Ta) and found that $V_{0.87}CoSb$ exhibited the highest zT value of 0.58 at 950 K. Finally, Huang *et al.*[57] synthesized an n-type Bi_2Se_2S-based TE material, which achieved a zT value of 1.13 at 773 K.

On the other hand, organic TE materials mainly consist of polymers, which are relatively inexpensive, recyclable and easily processable. In general, polymers possess low thermal and electrical conductivity, which have led in the past to low zT values.[58] Some examples of organic n-type TE materials are poly(nickel-ethylenetetrathiolate) (poly[K_x(Ni-ett)])[59] and perylene diimide (PDI).[60] In addition, carbon allotropes, such as fullerenes and carbon nanotubes have been studied in regard to their TE properties. Liu *et al.*[61] synthesized a fullerene (C_{60}) derivative with side chains, which exhibited a zT value of 0.34 at 393 K. The performance of organic TE materials can be enhanced by the fabrication of composite materials, which most commonly comprise of a polymer and an inorganic material. Examples of n-type composite TE materials are poly(vinylidene fluoride) (PVDF)/Ni nanowires[62] and polyethyleneimine (PEI)/poly(3,4-ethylenedioxythiophene) (PEDOT)/carbon nanotubes (CNTs).[63] More n-type TE materials (inorganic, organic and composite), their characteristics and applications can be found in the literature.[64–71]

3.2 p-type thermoelectric materials

Regarding the p-type TE materials, $(Bi, Sb)_2$–$(Se, Te)_3$-based alloys are the most commonly used inorganic materials at near-room temperatures. Fan *et al.*[72] reported a p-type $Bi_{0.4}Sb_{1.6}Te_3$ material obtained through melt spinning with an enhanced zT value of 1.8 at 316 K. Moreover, Goncalves *et al.*[73] fabricated a thin film of Sb_2Te_3 onto glass substrate, which achieved a Seebeck coefficient of 160 μV K^{-1} and a zT value of 0.3 at 300 K. Another class of p-type inorganic TE materials for low temperature applications are MgAgSb-based materials. For example, Liu *et al.*[74] tried to enhance the zT value by varying the Sb

content and concluded that the best formula is $MgAg_{0.97}Sb$. From mid to high temperatures, more suitable inorganic p-type materials are GeTe-based materials, like $Ge_{0.95}Bi_{0.05}Te_{1.025}$,[75] and $Ge_{0.9}Sb_{0.1}Te$,[76] copper and tin chalcogenides (Cu_2X or SnX, X = S, Se, Te), like Cu_2Se[77] and SnSe.[78]

Organic p-type TE materials like PEDOT[79] and polythiophene (PTh)[80] exhibit TE properties with values lower than their inorganic counterparts. Therefore, incorporating inorganic materials in polymer matrixes has proved to be an efficient strategy for enhancing the TE properties of these materials. Some examples of composite p-type TE materials are PEDOT:PSS/Bi_2Te_3,[81] PVDF/Cu_2Se[82] and PEDOT:PSS/SnSe.[83] Other p-type TE materials (inorganic, organic and composite) can be found in recent review papers.[68–71,84–86]

4. Lattice structures

Lattice structures, foams and honeycombs are referred to as *cellular structures*. Initially, Gibson[87] defined cellular structures as an interconnected network of struts or plates and extinguished them into honeycombs and foams. A honeycomb is a 2-D sketch of parallel prismatic cells extruded into the third dimension. Foams are polyhedral cells that form 3-D structures. Gibson categorized foams into *open-cell foams*, where struts form the edges of the cells, and *closed-cell foams*, in which the cell faces are covered by a membrane. Later, Ashby[88] introduced the term *lattice* as a synonym to *cellular* and emphasized on the importance of viewing lattice materials both as structures, like in structural engineering, but also as materials with their own properties, which are comparable to bulk monolithic materials.

Therefore, a lattice is defined as a three-dimensional structure with a periodic network of elements such as slender beams or rods.[89] Although the most well-known lattice structures are lattice trusses (*e.g.* octet-truss), other designs such as honeycombs and gyroids, also match the definition of lattices. In Fig. 1, illustrations of some lattice structures are presented. More lattice structures and their properties can be found in the literature.[90–93]

The most important structural property of lattice structures is their relative density, which is defined as the density of the lattice structure divided by the density of the base solid material. This ratio affects the mechanical properties and the behaviour of the lattice structures under mechanical stress. In 3D-printed lattice structures by the FDM- and DLP-technique, it has been shown that higher relative densities result in improved stiffness and strength.[94,95] Moreover, metal lattice structures fabricated by SLM exhibited a linear correlation between relative density and energy absorption.[96] In addition, compression tests concluded that specimens with higher relative densities experienced stretch-dominated deformation, while specimen with lower relative densities exhibited bending-dominated deformation. Although values of mechanical properties depend on many factors, such as the material, 3D-printing technique, lattice architecture *etc.*, the trend between relative density and mechanical properties remains the same. In Fig. 2, the correlation between mechanical properties and relative density is demonstrated.

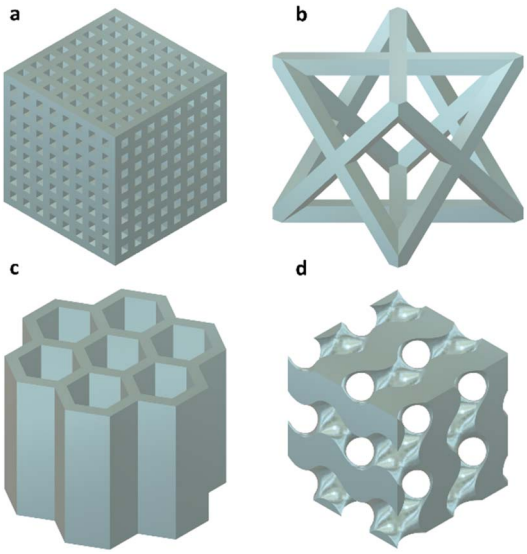

Fig. 1 Illustrations of some lattice structures. (a) Square lattice. (b) Face-centered cubic lattice. (c) Honeycomb-shaped lattice. (d) Gyroid.

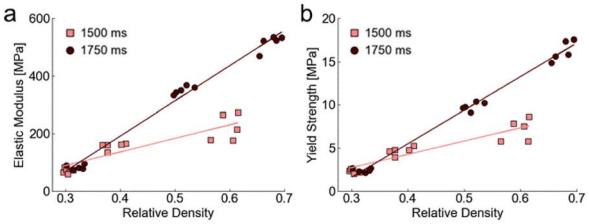

Fig. 2 Mechanical properties of the tested samples of different exposure times in relation to the relative density (a) elastic modulus and (b) yield strength. Reproduced with permission.[95] Copyright 2022, MDPI.

Another metric of the mechanical properties of lattice structures is the volume fraction. Volume fraction is defined as the volume percentage (vol%) of the solid material in the lattice structure and should not be confused with the relative density. Yan *et al.*[97] fabricated lattice structures *via* SLM and showed that higher volume fractions lead to enhanced compression strength and modulus.

The thermal properties of lattice structures have been studied both theoretically and experimentally by many scholars. Wang *et al.*[98] investigated the effective thermal conductivity of different lattice structures with various porosities through simulations and experiments. The lattice structures were additively manufactured for a single porosity value and the results of the measured effective thermal conductivity were in good agreement with the values obtained by the simulations. The authors concluded that the effective thermal conductivity of all examined topologies decreased with increasing porosity of the lattice structures. Takezawa *et al.*[99] optimized the lattice topology through simulations and 3D-printed the optimal lattice design by utilizing the SLM-technique. The results showed that the effective thermal conductivity increased with increasing volume fraction, while the bulk structure exhibited

the highest thermal conductivity. Moreover, Catchpole *et al.*[100] fabricated triply-periodic minimal surface (TPMS) lattice structures by SLM and tested their thermal performance in comparison to the volume fraction. The results showed a linear relationship between the volume fraction and the thermal conductivity of the lattices, which means that increasing volume fraction leads to increased thermal conductivity. In addition, Thimont and LeBlanc[101] showed that hollow TE leg geometries result in more effective heat resistance, *i.e.* higher temperature gradients.

All of the above studies agree to the fact that lattice structures exhibit reduced thermal conductivities in comparison to their monolithic bulk structures. Furthermore, it is apparent that low volume fraction of lattice structures leads to low thermal conductivity. Therefore, the implementation of lattice structures with low volume fraction could be advantageous in TE devices, since they could reduce the thermal conductivity in the device and lead to an enhanced performance (higher zT value). Finally, Zhang *et al.*[102] observed through simulations a 5-fold decrease in the effective thermal conductivity and a 6-fold increase in the power generated per 1 kg Bi_2Te_3, by replacing bulk cuboid TE legs with lattice-like TE legs.

As is evident from the above discussion, 3D lattice structures provide several advantages compared to bulk ones.[103,104] The ability to control the shape and morphology of the 3D structure offers the potential to control the thermal conductivity and mechanical stability of the 3D network and thus enhance the performance of the TE devices. Moreover, AM enables the printing of composite or even functionally graded TE materials[105] with improved TE properties.

However, a special case of 3D lattice structures that has the potential to revolutionize the field of thermoelectrics, by offering a distinct array of advantages that significantly enhance TE performance, are the core–cell configurations. A schematic illustration of core–shell configurations can be found in Fig. 3.

These structures consist of a core material enveloped by a shell, allowing for tailored properties that can optimize the efficiency of TE devices.[106–108] One of the primary advantages of core–shell structures, is the ability to manipulate thermal[109] and electrical transport properties independently. By assuming that k_1, k_2 and σ_1 and σ_2 are the thermal and the electrical conductivities of the shell and the core, respectively, then the effective thermal conductivity k_{eff} and the effective electrical conductivity σ_{eff} of the 3D lattice structure will depend not only on the material properties and the 3D structure design, but also on the geometrical characteristics (length and thickness) of the shell and the core. In a similar fashion, the effective Seebeck coefficient S_{eff} will depend on the Seebeck coefficients S_1 and S_2 of both the shell and the core. In this case, the figure of merit (zT) can be estimated by the following equation:

$$zT = \frac{{S_{\text{eff}}}^2 \times \sigma_{\text{eff}} \times T}{\kappa_{\text{eff}}}$$

Thus, core–shell structures offer additional degrees of freedom that could be exploited in order to optimize the figure of merit of the TE devices. The exact nature of the dependence of the effective coefficients k_{eff}, σ_{eff} and S_{eff} of the 3D structure on the coefficients of the constituting components, could be estimated by theoretical and computational analysis. Computer modeling could provide a valuable tool, in this case, for selecting the optimum geometrical characteristics of the 3D lattice structures.[110]

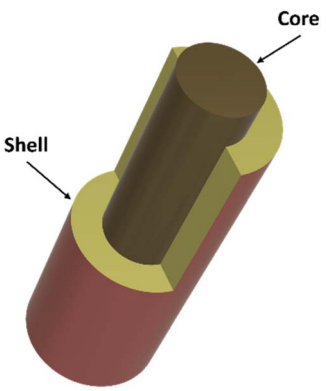

Fig. 3 Schematic illustration of the core–shell configuration.

5. 3D-printed lattice structures for thermoelectric devices

Conventional manufacturing processes (top–down) for mass production, include multiple steps, which limit the geometrical shape and size characteristics of the fabricated devices. Thus, AM techniques have been implemented, in order to provide flexibility in shape and allow customization of the devices in a cost-effective manner[111]. Although AM techniques have been utilised for over a decade for the fabrication of TEGs from bulk TE materials with simple (cuboid, disc *etc.*)[112,113] or more complex (arc-shaped, helix-shaped *etc.*)[114,115] geometries, lattice architectures have only recently started to attract the attention of the scientific community. Lattice-like device architectures provide weight and material cost reduction, while exhibiting improved TE properties.

There are some reviews[116–118] that address the utilisation of AM in the field of TE devices, but the majority of the referred TE devices consist of bulk- or dense-structured components. This review focuses exclusively on TE devices with lattice-structured TE legs, which have been fabricated by AM techniques. Within the scope of this review, the lattice structures are distinguished into two categories: (i) lattice structures with square or rectangular cross-section and (ii) lattice structures with miscellaneous cross-sections, *e.g.* honeycomb-shaped lattice. In the following sections, TEGs with lattice architectures fabricated by different AM techniques are reported.

5.1 Square/rectangular lattice structures

To the best of our knowledge Kim *et al.*[119] were the first to report the fabrication of a TEG with a lattice-like shape by using a 3D-printing technique. Specifically, an extrusion-based technique was used to fabricate $(Bi,Sb)_2(Te,Se)_3$-based TE legs in arch and

lattice form. DIW was utilised to 3D-print the prepared p- and n-type colloidal TE inks, which exhibited high viscoelasticity without the addition of organic binders. The p- and n-type TE inks consisted of $Bi_{0.55}Sb_{1.45}Te_3$ with 25 wt% $Sb_2Te_4^{2-}$-based chalcogenidometallate (ChaM) and $Bi_2Te_{2.7}Se_{0.3}$ with 10 wt% ChaM. The addition of ChaM contributes to the stability and printability of the ink by controlling the particle size, their size distribution and their surface oxidation. The 3D-printed structures were heat treated for 30 min at 450 °C under H_2 atmosphere (15% H_2, 85% Ar), which resulted in a 36% volume contraction. The TE properties of the p- and n-type inks were studied within the temperature range of 300–500 K. The Seebeck coefficient of the p-type ink showed a peak value of 217.5 μV K^{-1} at 425 K, while the n-type ink showed a peak value of 132.4 μV K^{-1} at 500 K. The peak values of PF were measured at 300 K and were 2.4 and 1.0 mW m^{-1} K^{-2} for p-type and n-type, respectively. Furthermore, the highest values of zT were achieved at 375 K for p-type inks ($zT = 1.0$) and at 425 K for n-type inks ($zT = 0.5$).

Kenel *et al.*[120] used an extrusion-based 3D-printing technique in order to fabricate Bi_2Te_3 TE legs. The ink containing Bi_2O_3, TeO_2 and a polymeric binder is extrusion-printed to form a microlattice with dimension 5 mm(L) × 5 mm(W) × 2 mm (H). Afterwards, two different processing routes were explored: (i) direct co-reduction in H_2, followed by elemental interdiffusion and formation of Bi_2Te_3 (coarse-grained) or (ii) pre-sintering in air, followed by co-reduction in H_2 and formation of Bi_2Te_3 (fine grained). The reduction in H_2 was executed in two steps, first for 2 h at 673 K and then for 1 h at 743 K. The pre-sintering in air at 773 K lasted 1 h. More details about the formation mechanism of the intermediaries and the final product of Bi_2Te_3 can be found on the full paper, since the synthesis process was studied by *in situ* synchroton X-ray diffraction. According to the authors, the processing route including pre-sintering in air, results in Bi_2Te_3 with significantly smaller pore and grain size than the direct co-reduction in H_2. Both the coarse-grained and the fine-gained showed similar electrical conductivities and Seebeck coefficients between 293 K and 523 K, but different thermal conductivities, with the thermal conductivity of the fine-grained sample being lower than the coarse grained. Due to the lower thermal conductivity, the fine-grained sample exhibited in the temperature range 373–423 K a zT value of ∼0.4, while the coarse-grained a zT value of ∼0.2.

Wang *et al.*[121] used a material-extrusion technique of TE inks to 3D-print a lattice structure with square cross-section. The lattice consisted of 9 layers one on top of another, with 1 cm × 1 cm plane size. The Bi_2Te_3-based inks were modified with (i) polyelectrolyte additives, which improved the stability and viscoelasticity of the inks and (ii) methylcellulose, which improved the mechanical properties of the structures. Apart from the periodic structure (lattice), the developed TE inks were used to 3D-print three pairs of p-type and n-type half rings (8 mm inner diameter, 15 mm outer diameter, 2 mm thickness), which were connected to form a TE generator. After 3D-printing, the structures were annealed at 450 °C for 2 h. The authors concluded that inks containing 0.9 wt% methylcellulose and 70.2 wt% TE material, exhibited the best stability and printability. The peak zT values for the p-type ($Bi_{0.5}Sb_{1.5}Te_3$) and n-type ($Bi_2Te_{2.7}Se_{0.3}$) structures were 0.65 at ∼450 K and 0.53 at −425 K, respectively.

Al Malki *et al.*[122] used a material-extrusion technique to 3D-print a micro-lattice with ∼600 μm diameter struts. Moreover, the authors prepared samples in the form of blocks by pouring ink in a Teflon mold (ink casting). The TE ink consisted of the n-type half-Heusler alloy $Nb_{1-x}CoSb$ and polystyrene as organic binder. The dimension of the micro-lattice was 25 mm(L) × 25 mm(W) × 5 mm(H) with a strut spacing of 2 mm and the dimension of the cast blocks 14 mm(L) × 14 mm(W) × 5 mm(H). After 3D-printing and ink casting, the samples were heat treated with a two-step debinding process (1 h at 423 K and 1 h at 723 K) under Ar atmosphere and sintered at 1373 K for 10 h under vacuum. Unfortunately, the TE properties were only measured for ink-cast samples, which exhibited a peak zT value of 0.10 ± 0.015 and Seebeck coefficient of −92 μV K^{-1} at 873 K. For comparison reasons, a hot-pressed sample was synthesized, which showed a zT value of ∼0.26 and Seebeck coefficient of −150 μV K^{-1} at 873 K.

Kim *et al.*[123] used an extrusion-based 3D printing process to fabricate a TEG with pin-shaped TE legs. Each TE leg of the TEG was constructed by multiple pins, with the optimal design being 20 pins for the p-type leg and 9 pins for the n-type. The dimensions of the legs were 11.33 mm(L) × 8.87 mm(W) × 10 mm(H) for the p-type and 4.03 mm(L) × 9.08 mm(W) × 10 mm(H) for the n-type. In Fig. 4, there is a schematic illustration of the fabrication process of the pin-shaped TE leg. After 3D-printing, the TE legs were sintered under N_2 atmosphere at different conditions, 5 h at 988 K for the n-type leg and 1 h at 803 K for the p-type. The n-type legs consisted of $AgBiSe_2$ and the p-type of $AgSbTe_2$. Moreover, the TE inks were developed using glycerol as dispersion medium and without any additives, which could potentially influence their electrical and thermal properties. The TE inks exhibited peak zT values of 0.49 for the n-type at 700 K and 1.20 for the p-type at 600 K. Moreover, the n-type TE legs achieved a Seebeck coefficient of −69.75 μV K^{-1} at room temperature and a PF of 2.76 μW cm^{-1} K^{-2} at 700 K. On the other hand, the p-type TE legs achieved a Seebeck coefficient of 253 μV K^{-1} at room temperature and a PF of 6.42 μW cm^{-1} K^{-2} at 600 K. For comparison reasons, a TEG with cuboid legs, but the same dimensions, was fabricated. The results showed that the pin-shaped TEG reached 25% higher ΔT than the TEG with cuboid legs, which translated into a higher output voltage

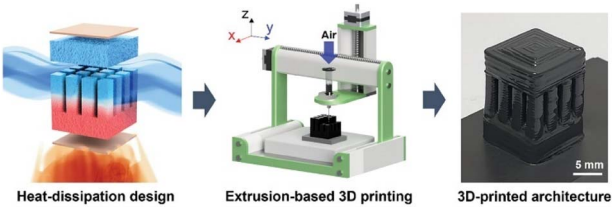

Fig. 4 Schematic showing of the overall processing for the fabrication of the heat-dissipation-designed TE leg. Reproduced with permission.[123] Copyright 2024, Wiley-VCH GmbH.

and output power by 16% and 80%, respectively. The authors concluded that the architecture of the legs significantly influences the efficiency of the TEG. In addition, the mechanical properties of the 3D-printed lattices were evaluated by uniaxial compression tests. Both $AgBiSe_2$ and $AgSbTe_2$ samples exhibited similar behavior, where increasing compressive strain led to increasing compressive stress until the point of material failure, which is characterized by a sudden decrease in compressive stress, indicating a direct brittle fracture. The compressive strength of $AgBiSe_2$ and $AgSbTe_2$ was found to be 324.0 MPa and 75.25 MPa, respectively. Furthermore, the Young's modulus was calculated for both samples, reaching a value of 14.34 GPa for $AgBiSe_2$ and 8.258 GPa for $AgSbTe_2$. According to the authors, the values of the Young's modulus are lower than those of other conventional bulk TE materials, but the values of compressive strength are similar or even higher.

5.2 Miscellaneous lattice structures

Choo *et al.*[124] was one of the first to utilize lattice-like 3D-printed TE legs. The TEGs consisted of a hollow hexagonal column- or a honeycomb-based single leg, which was fabricated by an extrusion-based technique of p-type Cu_2Se TE material. In Fig. 5, there is a scheme of the 3D-printing process. The 3D-printing colloidal inks were binder-free, due to the addition of inorganic Se_8^{2-} polyanion, which acted as a sintering promoting agent and improved printability. Optimal printing results, while avoiding nozzle plugging and obtaining structural integrity, were achieved with inks containing 50 wt% Se_8^{2-}. The developed inks showed a peak value of $zT = 1.21$ and Seebeck coefficient of 185.4 $\mu V\ K^{-1}$ at 1000 K. After printing, the samples were sintered at 873 K under a gas mixture atmosphere (96% N_2, 4% H_2) for different times. The best results were obtained for a sintering duration of 5 h. Regarding the dimension of the samples, the cross-sectional area was 4.0 mm^2 for the hexagonal-shaped leg and 105.21 mm^2 for the honeycomb-shaped leg, while the leg length and wall thickness of all TEGs was 6 mm and 0.33 mm respectively. Among the three different (cuboid, hollow hexagonal and honeycomb) module architectures, the honeycomb-based TE module showed the highest power, due to its cross-sectional area, which is larger in comparison to the other architectures and leads to a lower module resistance. The power density of the honeycomb-based TEG was 621.40 mW cm^{-2}. Moreover, the mechanical properties of the 3D-printed cuboid- and honeycomb-shaped legs were measured under uniaxial compression. Although both architectures exhibited similar behavior in the elastic region, the honeycomb-shaped leg exhibited a larger region of plastic deformation and higher fracture strain. According to the authors, the specific stiffness of the honeycomb architecture was found to be 198 kPa $m^3\ kg^{-1}$, which is greater than other materials with high specific stiffness.

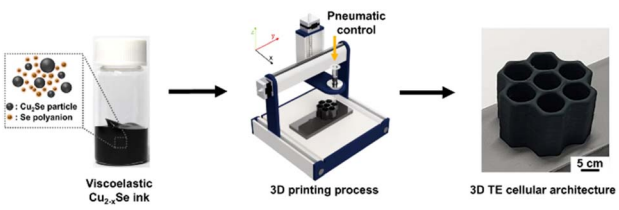

Fig. 5 Scheme for 3D printing process of the Cu_2Se-based honeycomb cellular architecture by using all-inorganic $Cu_{2-x}Se$ ink. Reproduced with permission.[124] Copyright 2021, Springer Nature.

Han *et al.*[105] used an extrusion-based 3D printing process to fabricate n-type $Bi_2Te_{2.7}Se_{0.3}$ TE legs. The formulated inks were doped with Na and included molecular anionic additives ($Sb_2Te_4^{2-}$), which improved the rheological properties. The Na-doped inks were 3D-printed in order to create a TE leg (FGTEM) with a void and doping gradient (increasing Na concentrations stepwise). The layer thickness was 150 μm and the x wt% Na doping ($x = 0$, 0.05, 0.1, 0.15, 0.2) increased from top to bottom. The void gradient varied from 0% to 60% in the vertical direction and the voids had 3 different shapes: (i) square, (ii) pentagon or (iii) hexagon. The dimension of the FGTEM was 2 mm(L) × 2 mm(W) × 1.5 mm(H). After sintering at 783 K for 3 h, the final dimension of the FGTEM was 1.4 mm(L) × 1.4 mm(W) × 1.0 mm(H), due to shrinkage. According to the measurements, the Seebeck coefficients at room temperature of Na-doped $Bi_2Te_{2.7}Se_{0.3}$ increased with increasing Na concentration, with the maximum value being −208 $\mu V\ K^{-1}$ for the sample with 0.2 wt% Na doping. On the other hand, the maximum value of PF (15 $\mu W\ cm^{-1}\ K^{-2}$ at room temperature) and zT (0.8 at 350 K) was achieved with 0.175 wt% Na-doping. Finally, a TEG was fabricated by combining an n-type multiply graded x wt% Na-doped $Bi_2Te_{2.7}Se_{0.3}$ leg ($x = 0$, 0.10, 0.175) and a p-type $Bi_ySb_{2-y}Te_3$ leg with a composition gradient ($y = 0.35$, 0.50, 0.55). For comparison reasons, a TEG consisting of homogenous $Bi_2Te_{2.7}Se_{0.3}$ doped with 0.175 wt% Na (n-type leg) and $Bi_{0.35}Sb_{1.65}Te_3$ (p-type leg) was fabricated. After 3D-printing, both the n-type and the p-type TE legs were sintered for 3 h under N_2 atmosphere at 783 K and 723 K, respectively. The dimension of the n-type leg was 5.23 (L) × 5.23 mm(W) × 5 mm(H) and of the p-type was 5 mm(L) × 5 mm(W) × 5 mm(H). Moreover, the n-type doping-variant TE leg showed a 10% increase in the zT value, in comparison to the homogeneous TE leg. The authors concluded that the TEG with the multiply graded n-type leg and the composition-gradient p-type leg, exhibited a maximum power density of 357 mW cm^{-2}, which is 20% higher than that of the homogeneous TEG. In addition, the mechanical properties of 0.10 wt% Na-doped and undoped 3D-printed samples were evaluated by compressive tests, which resulted in similar values of Young's modulus and compressive strength for both samples.

Hu *et al.*[125] fabricated a honeycomb-shaped single leg TEG by the SLM 3D-printing technique. The 3D-printed leg consisted of n-type $Bi_2Te_{2.7}Se_{0.3}$ TE material, which exhibited a peak value $zT = 1.33$ at 400 K. For practical reasons, the authors focused on the average value of zT (zT_{ave}) within the examined temperature range (300–500 K), which was $zT_{ave} = 1.23$. Moreover, the highest value of PF = 41.3 $\mu W\ cm^{-1}\ K^{-2}$ was achieved at 300 K. The printing system was equipped with a fiber laser (1064 nm, 100 W) and the experiments were performed under a high-purity liquid Ar atmosphere. The samples were then treated at 623 K for 24 h in a vacuum furnace. For comparison reasons,

a cuboid-shaped single leg TEG was fabricated. The dimension of the samples was 7 mm(L) × 7 mm(W) × 12.5 mm(H) and the wall thickness 1.5 mm. The results showed that the honeycomb-shaped TEG was more efficient than the cuboid-shaped TEG, while the measured energy conversion efficiency was 10.2% and 5.8%, respectively. In addition, the authors highlighted the reliable service durability of the honeycomb-shaped TEG, which showed no significant alterations in terms of resistance and output voltage after 60 h of continuous testing.

Karthikeyan *et al.*[126] fabricated a TE device consisting of 3D-printed legs. The legs exhibited a face-centered cubic (FCC)-like lattice geometry and were printed by utilising the DLP vat photopolymerization technique. The printed lattices were partially carbonized in an inert atmosphere for 4 h at 350 °C. Afterwards, a thin film of a TE material with a thickness of approximately 1 μm was deposited by thermal evaporation on the surface of the printed lattice, resulting in a core–shell structure. Depending on the thin film of the TE material, the 3D-printed legs had either n-type (Bi_2Te_3) or p-type (Sb_2Te_3) behaviour. The TE device consisted of multiple n-type and p-type units in an alternating manner, which means that they are electrically connected in series through nickel contacts, and thermally connected in parallel. The dimension of each TE unit was 5 mm(L) × 5 mm(W) × 5 mm(L). The TE units were placed between two electrically insulating alumina plates. A schematic illustration of the fabrication process of the FCC-like lattice and the TEG, as well as the unit cell and the resultant lattice, can be found in Fig. 6.

Regarding, the Seebeck coefficient of the n-type and p-type TE units in the temperature range of 300–550 K, they were found to be between 120–130 μV K^{-1} and 160–240 μV K^{-1}, respectively. According to the authors, the lattice structure of the TE legs resulted in a higher temperature difference between

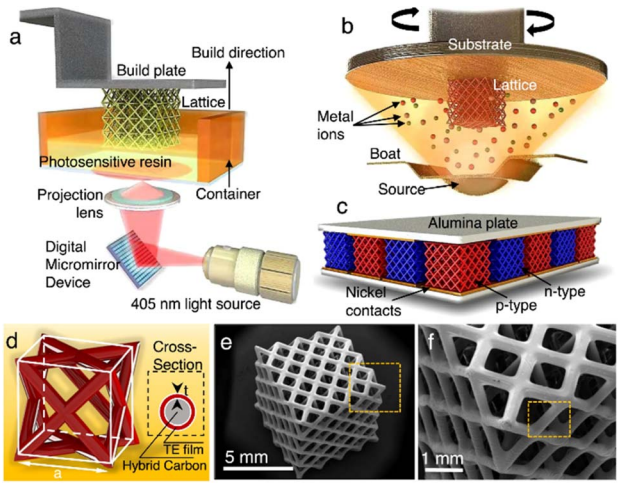

Fig. 6 Fabrication of 3D-printed TEGs. (a) Representation of the DLP fabrication process used to fabricate FCC-like lattices. (b) Illustration of the thermal evaporation process, which was used to deposit thin TE films on the 3D-printed lattice. (c) Illustration of the fabricated TEG. (d)–(f) Feature size of the unit cell used to create the lattice and the final result of the FCC-like lattice. Reproduced with permission.[126] Copyright 2023, Springer Nature.

Table 3 Overview of 3D-printed lattice structures for TE devices and their TE properties. In ref. 105, 119–121, 123, 124 and, 127 the TE material was incorporated in the printing material and was directly 3D-printed to form the lattice structure, while in ref. 125, the TE material was in powder form and was 3D-printed by SLM and in ref. 126, the TE material was applied as a thin film on the 3D-printed lattice structure by thermal evaporation

Printing method	TE material	TE type	Lattice	S (μV K^{-1})	zT	PF (μW cm^{-1} K^{-2})	Ref.
Direct ink writing	$Bi_2Te_{2.7}Se_{0.3}$ with 10 wt% $Sb_2Te_4^{2-}$	n	Square	(−)132.4 (500 K)	0.5 (425 K)	10 (300 K)	119
Direct ink writing	$Bi_{0.55}Sb_{1.45}Te_3$ with 25 wt% $Sb_2Te_4^{2-}$	p	Square	(+)217.5 (425 K)	1.0 (375 K)	24 (300 K)	119
Direct ink writing	Bi_2Te_3	n	Square	—	~0.4 (373–423 K)	—	120
Direct ink writing	$Bi_2Te_{2.7}Se_{0.3}$	n	Square	~(−)172 (~425 K)	0.53	—	121
Direct ink writing	$Bi_{0.5}Sb_{1.5}Te_3$	p	Square	~(+)169 (~450 K)	0.65	—	121
Direct ink writing	$AgBiSe_2$	n	Pin-shaped	(−)69.75 (298 K)	0.49 (700 K)	2.76 (700 K)	123
Direct ink writing	$AgSbTe_2$	p	Pin-shaped	(+)253 (298 K)	1.20 (600 K)	6.42 (700 K)	123
Direct ink writing	Cu_2Se	p	Honeycomb-shaped	(+)185.4 (1000 K)	1.21 (1000 K)	—	124
Direct ink writing	Na-doped $Bi_2Te_{2.7}Se_{0.3}$	n	Void-variant	(−)208 (298 K)	0.80 (350 K)	15 (298 K)	105
Selective-laser melting	$Bi_2Te_{2.7}Se_{0.3}$	n	Honeycomb-shaped	—	1.33 (400 K)	41.3 (300 K)	125
Vat photopolymerization	Bi_2Te_3	n	Face-centered cubic	(−)130 (350 K)	1.09 (550 K)	7.0	126
Vat photopolymerization	Sb_2Te_3	p	Face-centered cubic	(+)235 (350 K)	0.97 (550 K)	6.4	126
Direct ink writing	$Bi_{0.5}Sb_{1.5}Te_3$	p	Gyroid lattice	—	0.187 (435 K)	0.375 (435 K)	127

the hot- and cold-side, which yielded high zT values at 550 K for both the n-type ($zT = 1.09$) and the p-type ($zT = 0.97$). Moreover, the peak value of PF was 7 μW cm^{-1} K^{-2} for the n-type TE unit and 6.4 μW cm^{-1} K^{-2} for the p-type. Furthermore, the mechanical properties of the core–shell TE lattices were evaluated by uniaxial compression tests with up to 50% strain. The results showed an enhanced compressive modulus (~450 MPa) and strength (~35 MPa). In addition, the TE lattices retained most of their electrical properties even after deformations with strain up to 75%. By comparing the results with other values reported in the literature, the authors concluded that their core–shell TE lattices outperform many bulk TE materials and other ductile lattice structures in terms of strength per unit density and ductility.

Zhang *et al.*[127] used an extrusion-based technique in order to fabricate porous 3D TEGs with gyroid structures. The DIW technique was utilized to 3D-print the prepared p-type TE inks, consisting of 70 wt% $Bi_{0.5}Sb_{1.5}Te_3$ powder dispersed in a 25 wt% Pluronic F127 aqueous solution. Pluronic F127 systems can behave either as a sol or a gel, depending on the temperature of their environment. The developed ink behaved as a gel when $T > T_{gel} = 14.3$ °C, thus enabling its 3D-printing application at room temperature. The 3D-printed gyroid structures were subject to heat treatment at 500 °C or 550 °C for different durations in a gas mixture atmosphere (5% H_2, 95% N_2), which led to the thermal decomposition of Pluronic F127. The highest Seebeck coefficient and zT value were measured for the 3D-printed gyroid structures that were sintered at 500 °C for 10 h. The maximum value of $zT = 0.187$ and PF = 37.5 μW m^{-1} K^{-2} were achieved at 435 K.

Table 3 summarizes the characteristics and TE properties of the 3D-printed lattice structures that are used in thermoelectric devices.

6. Outlook

AM is transforming the field of TE devices by offering design freedom. While research on new TE materials continues, new device architectures are necessary in order to maximize the efficiency of TEGs. The application of lattice structures in TEGs has proved to be beneficial in terms of efficiency, since it could assist in the decoupling of competing TE properties, like the Seebeck coefficient and the thermal conductivity. On the other hand, one major drawback of lattice structures in most cases is the lower mechanical strength in comparison to their bulk monolithic counterparts. Apparently, the mechanical strength of the 3D-printed lattice-like legs influences the stability and operability of TEGs, where a high mechanical strength is desired in order to ensure the long-term service of the devices. Some researchers[105,123–126] have studied the mechanical properties of TE devices consisting of 3D-printed lattice structures, indicating promising results. However, further research is necessary in order to address this issue and extract safe results over the long-term effects of the various stresses that are being applied on TEGs. To conclude, it is important to find the golden ratio between mechanical properties and device efficiency, according to the requirements of each application.

Although new architectures, like lattice structures, are starting to get integrated in TE devices, the materials remain the same. In all the above outlined cases with lattice structures, the TE materials are inorganic. Therefore, future research needs to focus on the development of sustainable materials, which are also less toxic. Despite composite and organic TE materials offering a good alternative to their inorganic counterparts, research needs to progress, since their efficiency (zT value) is still low.

Yet another challenge is the optimal integration of these materials in the new architectures of the TE devices. There are many strategies through which this could be achieved. One way could be the incorporation of TE materials in the printing materials and then directly 3D-print the desired structure. Another strategy could be through a core–shell structure, where the core consists of a standard 3D-printing material and the shell of the desired TE material. There are many post-processing techniques that could be utilised in order to apply a thin film of a TE material onto an already 3D-printed structure.

Moreover, advances in many AM technologies, like TPP, have enabled the fabrication of structures with feature sizes at the nanometer scale, providing even more topological freedom than before. Therefore, future research should focus on the optimization of the lattice design and size. There are many lattice designs available for experimentation, some simple (*e.g.* square or rectangular) and other more complex (*e.g.* gyroid or Schwarz lattice), which need to be evaluated in terms of their efficiency and practical implementation.

Data availability

All data and figures contained in this review article are from published articles that have been referenced in the article.

Author contributions

Data analysis and visualization (S. N. K.); manuscript writing – original draft (S. N. K.); conceptualization (S. N. K., C. T.); funding, project supervision (C. T.); manuscript writing–review & editing (S. N. K., C. T.).

Conflicts of interest

There are no conflicts to declare.

Acknowledgements

This work was supported by the Institute of Nanoscience and Nanotechnology of NCSR "Demokritos".

Notes and references

1 D. M. Rowe, *CRC Handbook of Thermoelectrics*, CRC Press, 1st edn, 1995.
2 W. Brostow, T. Datashvili, H. E. Hagg Lobland, T. Hilbig, L. Su, C. Vinado and J. White, *J. Mater. Res.*, 2012, **27**, 2930–2936.

3 S. Wei, X. Huang, L. Deng, Z.-C. Yan and G. Chen, *Compos. Sci. Technol.*, 2021, **208**, 108759.
4 T. G. Novak, K. Kim and S. Jeon, *Nanoscale*, 2019, **11**, 19684–19699.
5 M. Aljaghtham, *Energy Rep.*, 2024, **11**, 859–876.
6 O. Nelson-Dummett, T. Whittaker, W. Whittow, J. Wojcik, J. F. Reyes Luna, C. McCall, A. Koca, C. J. Tuck, R. J. M. Hague and L. Turyanska, *Mater. Today Adv.*, 2025, **26**, 100584.
7 M. S. Saleh, C. Hu, J. Brenneman, A. M. Al Mutairi and R. Panat, *Addit. Manuf.*, 2021, **39**, 101856.
8 C. Hu, S. Jahan, B. Yuan and R. Panat, *Adv. Sci.*, 2025, **12**, 2405334.
9 I. Gibson, D. Rosen, B. Stucker and M. Khorasani, *Additive Manufacturing Technologies*, Springer, 3rd edn, 2021.
10 S. Wang, Y. Yu, H. Liu, K. T. P. Lim, B. M. Srinivasan, Y. W. Zhang and J. K. W. Yang, *Nano Futur.*, 2018, **2**, 025006.
11 M. S. Hossain, T. Li, Y. Yu, J. Yong, J.-H. Bahk and E. Skafidas, *RSC Adv.*, 2020, **10**, 8421–8434.
12 M. Burton, G. Howells, J. Atoyo and M. Carnie, *Adv. Mater.*, 2022, **34**, 2108183.
13 A. Sarbajna, A. G. Rösch, L. Franke, U. Lemmer and M. M. Mallick, *Adv. Eng. Mater.*, 2023, **25**, 2200980.
14 M. Hong, S. Sun, W. Lyu, M. Li, W. Liu, X.-L. Shi and Z.-G. Chen, *Soft Sci.*, 2023, **3**, 29.
15 T. Rodrigues-Marinho, N. Perinka, P. Costa and S. Lanceros-Mendez, *Mater. Today Sustain.*, 2023, **21**, 100292.
16 N. Singh, H. Siddiqui, B. S. R. Koyalada, A. Mandal, V. Chauhan, S. Natarajan, S. Kumar, M. Goswami and S. Kumar, *Met. Mater. Int.*, 2023, **29**, 2119–2136.
17 A. Das, D. Ghosh, S.-F. Lau, P. Srivastava, A. Ghosh and C.-F. Ding, *Adv. Eng. Inform.*, 2024, **62**, 102932.
18 Y. Wang, Y. Ding, K. Yu and G. Dong, *Polym. Compos.*, 2024, **45**, 15389–15420.
19 L. Zhou, J. Miller, J. Vezza, M. Mayster, M. Raffay, Q. Justice, Z. Al Tamimi, G. Hansotte, L. D. Sunkara and J. Bernat, *Sensors*, 2024, **24**, 2668.
20 W. Yanqing, W. Yuanchunzhi, C. Kehan, X. Lingan, F. Wei, C. He, Z. Xiang and L. Qinggang, *Int. J. Adv. Manuf. Technol.*, 2025, **136**, 4649–4675.
21 X. Zhou, L. Ren, Q. Liu, Z. Song, Q. Wu, Y. He, B. Li and L. Ren, *Macromol. Biosci.*, 2022, **22**, 2100332.
22 C. Pearson, S. Hawi, C. Lira, S. Goel and H. Yazdani Nezhad, *Mater. Today Proc.*, 2022, **64**, 1403–1411.
23 A. Reizabal, B. Tandon, S. Lanceros-Méndez and P. D. Dalton, *Small*, 2023, **19**, 2205255.
24 S. Bi, R. Wang, X. Han, Y. Wang, D. Tan, B. Shi, C. Jiang, Z. He and K. Asare-Yeboah, *Coatings*, 2023, **13**, 1150.
25 O. Bouzaglou, O. Golan and N. Lachman, *Polymers*, 2023, **15**, 2280.
26 M. Enyan, J. N. O. Amu-Darko, E. Issaka and O. J. Abban, *Eng. Res. Express*, 2024, **6**, 012401.
27 J. Jacob, D. Pejak Simunec, A. E. Z. Kandjani, A. Trinchi and A. Sola, *Technologies*, 2024, **12**, 267.
28 S. Ali, I. Deiab and S. Pervaiz, *Int. J. Adv. Manuf. Technol.*, 2024, **135**, 5085–5113.
29 M. K. Agarwala, V. R. Jamalabad, N. A. Langrana, A. Safari, P. J. Whalen and S. C. Danforth, *Rapid Prototyp. J.*, 1996, **2**, 4–19.
30 J. A. Lewis, *Adv. Funct. Mater.*, 2006, **16**, 2193–2204.
31 M. Zeng and Y. Zhang, *J. Mater. Chem. A*, 2019, **7**, 23301–23336.
32 A. Afridi, A. Al Rashid and M. Koç, *Bioprinting*, 2024, **43**, e00360.
33 L. Wu and Y. Song, *Mater. Horiz.*, 2025, **12**, 401–417.
34 A. Husna, S. Ashrafi, A. A. Tomal, N. T. Tuli and A. Bin Rashid, *Hybrid Adv.*, 2024, **7**, 100307.
35 X. Wang, M. Jiang, Z. Zhou, J. Gou and D. Hui, *Composites, Part B*, 2017, **110**, 442–458.
36 Z. Gan, Y. Cao, R. A. Evans and M. Gu, *Nat. Commun.*, 2013, **4**, 2061.
37 S. Juodkazis, V. Mizeikis, K. K. Seet, M. Miwa and H. Misawa, *Nanotechnology*, 2005, **16**, 846–849.
38 H. M. Yehia, A. Hamada, T. A. Sebaey and W. Abd-Elaziem, *J. Manuf. Mater. Process.*, 2024, **8**, 197.
39 M. Mehrpouya, D. Tuma, T. Vaneker, M. Afrasiabi, M. Bambach and I. Gibson, *Rapid Prototyp. J.*, 2022, **28**, 1–19.
40 S. Fatemeh Nabavi, A. Farshidianfar and H. Dalir, *Opt. Laser Technol.*, 2025, **180**, 111480.
41 R. C. Crafer and P. J. Oakley, *Laser Processing in Manufacturing*, Springer, 1st edn, 1992.
42 X. Shi, L. Chen and C. Uher, *Int. Mater. Rev.*, 2016, **61**, 379–415.
43 Y. Tian, G.-K. Ren, Z. Wei, Z. Zheng, S. Deng, L. Ma, Y. Li, Z. Zhou, X. Chen, Y. Shi and Y.-H. Lin, *Renewable Energy*, 2024, **226**, 120443.
44 Q.-Y. Liu, X.-L. Shi, T.-Y. Cao, W.-Y. Chen, L. Li and Z.-G. Chen, *Prog. Mater. Sci.*, 2025, **150**, 101420.
45 J. He, K. Li, L. Jia, Y. Zhu, H. Zhang and J. Linghu, *Appl. Therm. Eng.*, 2024, **236**, 121813.
46 S. Asadikouhanjani, A. Zolfagharian and M. Bodaghi, *Adv. Eng. Mater.*, 2024, **26**, 2301609.
47 H. J. Goldsmid and R. W. Douglas, *Br. J. Appl. Phys.*, 1954, **5**, 386–390.
48 J. P. Heremans, V. Jovovic, E. S. Toberer, A. Saramat, K. Kurosaki, A. Charoenphakdee, S. Yamanaka and G. J. Snyder, *Science*, 2008, **321**, 554–557.
49 M. Hong, T. C. Chasapis, Z.-G. Chen, L. Yang, M. G. Kanatzidis, G. J. Snyder and J. Zou, *ACS Nano*, 2016, **10**, 4719–4727.
50 M. Tan, W.-D. Liu, X.-L. Shi, H. Gao, H. Li, C. Li, X.-B. Liu, Y. Deng and Z.-G. Chen, *Small Methods*, 2019, **3**, 1900582.
51 Y. Ding, Y. Qiu, K. Cai, Q. Yao, S. Chen, L. Chen and J. He, *Nat. Commun.*, 2019, **10**, 841.
52 L.-D. Zhao, S.-H. Lo, Y. Zhang, H. Sun, G. Tan, C. Uher, C. Wolverton, V. P. Dravid and M. G. Kanatzidis, *Nature*, 2014, **508**, 373–377.
53 A. T. Duong, V. Q. Nguyen, G. Duvjir, V. T. Duong, S. Kwon, J. Y. Song, J. K. Lee, J. E. Lee, S. Park, T. Min, J. Lee, J. Kim and S. Cho, *Nat. Commun.*, 2016, **7**, 13713.
54 K. Kihou, H. Kunioka, H. Nishiate and C. H. Lee, *J. Mater. Res. Technol.*, 2021, **10**, 438–444.

55 S. Ren and L. Gou, *Adv. Appl. Ceram.*, 2021, **120**, 95–103.
56 D. A. Ferluccio, J. E. Halpin, K. L. MacIntosh, R. J. Quinn, E. Don, R. I. Smith, D. A. MacLaren and J.-W. G. Bos, *J. Mater. Chem. C*, 2019, **7**, 6539–6547.
57 K. Huang, Z.-Y. Wang, T.-Y. Zhong, Y.-X. Zhang, L. Yu, X. Yan, Y.-H. Jiang, Z.-H. Ge and J. Feng, *J. Eur. Ceram. Soc.*, 2025, **45**, 117192.
58 H. Yao, Z. Fan, H. Cheng, X. Guan, C. Wang, K. Sun and J. Ouyang, *Macromol. Rapid Commun.*, 2018, **39**, 1700727.
59 Y. Sun, L. Qiu, L. Tang, H. Geng, H. Wang, F. Zhang, D. Huang, W. Xu, P. Yue, Y. Guan, F. Jiao, Y. Sun, D. Tang, C. Di, Y. Yi and D. Zhu, *Adv. Mater.*, 2016, **28**, 3351–3358.
60 B. Russ, *Adv. Mater.*, 2014, **26**, 3473–3477.
61 J. Liu, B. Van Der Zee, R. Alessandri, S. Sami, J. Dong, M. I. Nugraha, A. J. Barker, S. Rousseva, L. Qiu, X. Qiu, N. Klasen, R. C. Chiechi, D. Baran, M. Caironi, T. D. Anthopoulos, G. Portale, R. W. A. Havenith, S. J. Marrink, J. C. Hummelen and L. J. A. Koster, *Nat. Commun.*, 2020, **11**, 5694.
62 Y. Chen, M. He, B. Liu, G. C. Bazan, J. Zhou and Z. Liang, *Adv. Mater.*, 2017, **29**, 1604752.
63 L. Wang, J. Zhang, Y. Guo, X. Chen, X. Jin, Q. Yang, K. Zhang, S. Wang and Y. Qiu, *Carbon*, 2019, **148**, 290–296.
64 A. Tripathi, Y. Lee, S. Lee and H. Y. Woo, *J. Mater. Chem. C*, 2022, **10**, 6114–6140.
65 Y. Zhang, Y. Wang, C. Gao, Z. Ni, X. Zhang, W. Hu and H. Dong, *Chem. Soc. Rev.*, 2023, **52**, 1331–1381.
66 M. Li and Dr Z. Shi, *ChemPlusChem*, 2023, **88**, e202300215.
67 S. Darabi, C.-Y. Yang, Z. Li, J.-D. Huang, M. Hummel, H. Sixta, S. Fabiano and C. Müller, *Adv. Electron. Mater.*, 2023, **9**, 2201235.
68 Y. Bao, Y. Sun, F. Jiao and W. Hu, *Adv. Electron. Mater.*, 2023, **9**, 2201310.
69 G. Rogl and P. F. Rogl, *Crystals*, 2023, **13**, 1152.
70 M. Yu, H. Li, Y. Li, S. Wang, Q. Li, Y. Wang, B. Li, K. Zhu and W. Liu, *EnergyChem*, 2024, **6**, 100123.
71 H. Cheng, Z. Wang, Z. Guo, J. Lou, W. Han, J. Rao and F. Peng, *Int. J. Biol. Macromol.*, 2024, **275**, 132908.
72 S. Fan, J. Zhao, J. Guo, Q. Yan, J. Ma and H. H. Hng, *Appl. Phys. Lett.*, 2010, **96**, 182104.
73 L. M. Goncalves, P. Alpuim, A. G. Rolo and J. H. Correia, *Thin Solid Films*, 2011, **519**, 4152–4157.
74 Z. Liu, J. Shuai, J. Mao, Y. Wang, Z. Wang, W. Cai, J. Sui and Z. Ren, *Acta Mater.*, 2016, **102**, 17–23.
75 D. Wu, L. Xie, X. Xu and J. He, *Adv. Funct. Mater.*, 2019, **29**, 1806613.
76 S. Perumal, S. Roychowdhury, D. S. Negi, R. Datta and K. Biswas, *Chem. Mater.*, 2015, **27**, 7171–7178.
77 K. Zhao, H. Duan, N. Raghavendra, P. Qiu, Y. Zeng, W. Zhang, J. Yang, X. Shi and L. Chen, *Adv. Mater.*, 2017, **29**, 1701148.
78 X. Shi, A. Wu, W. Liu, R. Moshwan, Y. Wang, Z.-G. Chen and J. Zou, *ACS Nano*, 2018, **12**, 11417–11425.
79 D. K. Taggart, Y. Yang, S.-C. Kung, T. M. McIntire and R. M. Penner, *Nano Lett.*, 2011, **11**, 125–131.
80 Y. Hu, H. Shi, H. Song, C. Liu, J. Xu, L. Zhang and Q. Jiang, *Synth. Met.*, 2013, **181**, 23–26.
81 L. Wang, Z. Zhang, Y. Liu, B. Wang, L. Fang, J. Qiu, K. Zhang and S. Wang, *Nat. Commun.*, 2018, **9**, 3817.
82 S. V. N. Pammi, V. Jella, J.-S. Choi and S.-G. Yoon, *J. Mater. Chem. C*, 2017, **5**, 763–769.
83 H. Ju and J. Kim, *ACS Nano*, 2016, **10**, 5730–5739.
84 Q. Shi, J. Li, X. Zhao, Y. Chen, F. Zhang, Y. Zhong and R. Ang, *ACS Appl. Mater. Interfaces*, 2022, **14**, 49425–49445.
85 W.-N. Wu, Q.-B. Zheng and C.-L. Liu, *Synth. Met.*, 2024, **307**, 117682.
86 J. Fu, S. Zhang, L. Liang, C. Du, Z. Ye and G. Chen, *Chin. Chem. Lett.*, 2024, **35**, 109804.
87 L. J. Gibson, *Mater. Sci. Eng., A*, 1989, **110**, 1–36.
88 M. F. Ashby, *Philos. Trans. Rozal Soc. A*, 2006, **364**, 15–30.
89 N. A. Fleck, V. S. Deshpande and M. F. Ashby, *Proc. R. Soc. Math. Phys. Eng. Sci.*, 2010, **466**, 2495–2516.
90 G. P. Borikar, A. R. Patil and S. B. Kolekar, *Int. J. Precis. Eng. Manuf.*, 2023, **24**, 2133–2180.
91 M. I. Chibinyani, T. C. Dzogbewu, M. Maringa and A. Muiruri, *Appl. Sci.*, 2024, **14**, 1582.
92 Y. Liu, T. Wang, H. Chen, Z. Li, S. Li, D. Wang, Y. Wang and K. Kosiba, *Int. J. Impact Eng.*, 2024, **191**, 104992.
93 C. Bhat, M. J. Prajapati, A. Kumar and J.-Y. Jeng, *Materials*, 2024, **17**, 3398.
94 J. León-Becerra, O. A. González-Estrada and J. Quiroga, *ACS Omega*, 2021, **6**, 29830–29838.
95 P. F. Egan, N. R. Khatri, M. A. Parab and A. M. E. Arefin, *Polymers*, 2022, **14**, 5515.
96 P. Płatek, J. Sienkiewicz, J. Janiszewski and F. Jiang, *Materials*, 2020, **13**, 2204.
97 C. Yan, L. Hao, A. Hussein, P. Young and D. Raymont, *Mater. Des.*, 2014, **55**, 533–541.
98 N. Wang, I. Kaur, P. Singh and L. Li, *Appl. Therm. Eng.*, 2021, **187**, 116558.
99 A. Takezawa, M. Kobashi, Y. Koizumi and M. Kitamura, *Int. J. Heat Mass Tran.*, 2017, **105**, 564–572.
100 S. Catchpole-Smith, R. R. J. Sélo, A. W. Davis, I. A. Ashcroft, C. J. Tuck and A. Clare, *Addit. Manuf.*, 2019, **30**, 100846.
101 Y. Thimont and S. LeBlanc, *J. Appl. Phys.*, 2019, **126**, 095101.
102 D. Zhang, N. Ngoh Yen Qi, S. Faye Duran Solco, X. Li and A. Suwardi, *ACS Energy Lett.*, 2024, **9**, 2240–2247.
103 J. U. Surjadi, L. Gao, H. Du, X. Li, X. Xiong, N. X. Fang and Y. Lu, *Adv. Eng. Mater.*, 2019, **21**, 1800864.
104 X. Feng, J. U. Surjadi, R. Fan, X. Li, W. Zhou, S. Zhao and Y. Lu, *Mater. Today*, 2021, **42**, 10–16.
105 H. Han, S. Eun Yang, J. Lee, K. Kim, C. Nam, S. Jo, S.-H. Lee, J.-Y. Kim, S. Ahn and J. Sung Son, *Chem. Eng. J.*, 2024, **497**, 154547.
106 J. Zhang, S. Li, Z. Zhu, Z. Wu and J. Zhang, *Dalton Trans.*, 2021, **50**, 10515–10523.
107 C. Li, X. Lan, P. Liu, J. Xu, Q. Jiang, C. Liu, C. Liu and F. Jiang, *Nano Res.*, 2023, **16**, 5702–5708.
108 R. Mulla and C. W. Dunnill, *Mater. Adv.*, 2022, **3**, 125–141.
109 W.-X. Zhou and K.-Q. Chen, *Sci. Rep.*, 2014, **4**, 7150.
110 L. Moreno-Sanabria, C. Ramírez, M. I. Osendi, M. Belmonte and P. Miranzo, *Addit. Manuf.*, 2024, **81**, 104018.

111 T. D. Ngo, A. Kashani, G. Imbalzano, K. T. Q. Nguyen and D. Hui, *Composites, Part B*, 2018, **143**, 172–196.
112 M. He, Y. Zhao, B. Wang, Q. Xi, J. Zhou and Z. Liang, *Small*, 2015, **11**, 5889–5894.
113 J. Qiu, Y. Yan, T. Luo, K. Tang, L. Yao, J. Zhang, M. Zhang, X. Su, G. Tan, H. Xie, M. G. Kanatzidis, C. Uher and X. Tang, *Energy Environ. Sci.*, 2019, **12**, 3106–3117.
114 M. Bian, Z. Xu, X. Tang, H. Jia, Y. Wang and A. Cabot, *J. Alloys Compd.*, 2024, **976**, 173202.
115 K. Song, G. Xu, A. N. M. Tanvir, K. Wang, M. O. Bappy, H. Yang, W. Shang, L. Zhou, A. W. Dowling, T. Luo and Y. Zhang, *J. Mater. Chem. A*, 2024, **12**, 21243–21251.
116 S. E. Yang, H. Han and J. S. Son, *JPhys Energy*, 2024, **6**, 022003.
117 J. Bi, Z. Liu, B. Li, S. Li, Z. Yang, M. D. Starostenkov and G. Dong, *J. Mater. Sci.*, 2024, **59**, 359–381.
118 Y. Du, J. Chen, Q. Meng, Y. Dou, J. Xu and S. Z. Shen, *Vacuum*, 2020, **178**, 109384.
119 F. Kim, S. E. Yang, H. Ju, S. Choo, J. Lee, G. Kim, S. Jung, S. Kim, C. Cha, K. T. Kim, S. Ahn, H. G. Chae and J. S. Son, *Nat. Electron.*, 2021, **4**, 579–587.
120 C. Kenel, M. M. F. Al Malki and D. C. Dunand, *Acta Mater.*, 2021, **221**, 117422.
121 Z. Wang, W. Cui, H. Yuan, X. Kang, Z. Zheng, W. Qiu, Q. Hu, J. Tang and X. Cui, *Mater. Today Energy*, 2023, **31**, 101206.
122 M. M. A. Malki, G. J. Snyder and D. C. Dunand, *Addit. Manuf. Lett.*, 2023, **4**, 100113.
123 K. Kim, S. Choo, J. Lee, H. Ju, S. Jung, S. Jo, S.-H. Lee, S. Baek, J.-Y. Kim, K. T. Kim, H. G. Chae and J. S. Son, *Adv. Sci.*, 2024, **11**, 2402934.
124 S. Choo, F. Ejaz, H. Ju, F. Kim, J. Lee, S. E. Yang, G. Kim, H. Kim, S. Jo, S. Baek, S. Cho, K. Kim, J.-Y. Kim, S. Ahn, H. G. Chae, B. Kwon and J. S. Son, *Nat. Commun.*, 2021, **12**, 3550.
125 Q. Hu, D. Luo, J. Guo, W. Qiu, X. Wu, L. Yang, Z. Wang, X. Cui and J. Tang, *ACS Appl. Mater. Interfaces*, 2023, **15**, 1296–1304.
126 V. Karthikeyan, J. U. Surjadi, X. Li, R. Fan, V. C. S. Theja, W. J. Li, Y. Lu and V. A. L. Roy, *Nat. Commun.*, 2023, **14**, 2069.
127 D. Zhang, X. J. G. Lim, X. Li, K. Saglik, S. F. D. Solco, X. Y. Tan, Y. Leow, W. Zhai, C. K. I. Tan, J. Xu and A. Suwardi, *ACS Energy Lett.*, 2023, **8**, 332–338.